PLATO camera ghosts: simulations and measurements on the engineering model (EM)

Martin Pertenais, Mathhias Ammler-von Eiff, Matteo Burresi, Juan Cabrera, Jacopo Farinato, et al.

Martin Pertenais, Mathhias Ammler-von Eiff, Matteo Burresi, Juan Cabrera, Jacopo Farinato, Nicolas Gorius, Rik Huygen, Demetrio Magrin, Cesar Martin Garcia, Matteo Munari, Sara Regibo, Pierre Royer, Bart Vandenbussche, Tim A. van Kempen, "PLATO camera ghosts: simulations and measurements on the engineering model (EM)," Proc. SPIE 12180, Space Telescopes and Instrumentation 2022: Optical, Infrared, and Millimeter Wave, 121804M (27 August 2022); doi: 10.1117/12.2629189

SPIE.

Event: SPIE Astronomical Telescopes + Instrumentation, 2022, Montréal, Québec, Canada

PLATO Camera Ghosts: simulations and measurements on the Engineering Model (EM).

Martin Pertenais[a], Matthias Ammler-von Eiff[b], Matteo Burresi[c], Juan Cabrera[d], Jacopo Farinato[e], Nicolas Gorius[f], Rik Huygen[g], Demetrio Magrin[e], Cesar Martin Garcia[d], Matteo Munari[f], Sara Regibo[g], Pierre Royer[g], Bart Vandenbussche[g], and Tim A. van Kempen[h]

[a]German Aerospace Center (DLR), Institute of Optical Sensor Systems, Rutherfordstr. 2, 12489 Berlin, Germany
[b]Max Planck Institute for Solar System Research, Justus-von-Liebig-Weg 3, 37077 Göttingen, Germany
[c]Leonardo Company, Via Delle Officine Galileo, Campi Bisenzio, Italy
[d]German Aerospace Center (DLR), Institute of Planetary Research, Rutherfordstr. 2, 12489 Berlin, Germany
[e]INAF - Osservatorio Astronomico di Padova, Vicolo dell'Osservatorio 5, 35122, Padova, Italy
[f]INAF - Osservatorio Astrofisico di Catania, Via S.Sofia 78, 95123, Catania, Italy
[g]Institute of Astronomy, KU Leuven, Celestijnenlaan 200D bus 2401, 3001 Leuven, Belgium
[h]SRON Netherlands Institute for Space Research, Niels Bohrweg 4, 2333 CA, Leiden, Netherlands

ABSTRACT

The PLAnetary Transits and Oscillations of stars mission (PLATO) is the M3 mission in ESA's Cosmic Vision 2015-2025 Programme, see Rauer et al. (2014).[1] The PLATO mission aims at detecting and characterizing extrasolar planetary systems, including terrestrial exoplanets around bright solar-type stars up to the habitable zone. To be able to perform the required high precision photometric monitoring of the large target stars sample, PLATO is based on a multi-telescope configuration consisting of 26 Cameras, so as to provide simultaneously a large field of view and a large collecting aperture. The optical design is identical for all cameras and consists of a 6-lens dioptric design with a 120 mm entrance pupil and an effective field of view of more than 1000 square degrees. As for every optical system, especially dioptric ones, the presence of optical ghosts can dramatically affect the scientific observations. Thanks to the application of an excellent anti-reflection coating, PLATO's cameras are by design very insensitive to ghosts. However, the residual faint back reflections focused on the detectors have to be simulated and considered during science operation (target selection) and in data correction algorithms.

This article describes the different optical analyses performed to estimate the importance of ghosts in PLATO's cameras, as well as the simulations performed to support the preparation of the test campaign on the first PLATO camera: the engineering model. Finally, the test execution, data analysis and results are presented and compared to the simulated data.

Keywords: exoplanet, AIT, PLATO, ghost, straylight

1. INTRODUCTION AND CONTEXT

1.1 PLATO Mission and Payload description

The PLATO payload is made of 24 identical "normal" cameras (N-CAM), 2 "fast" cameras (F-CAM), Ancillary Electrical Units providing electrical power and synchronisation signals to all cameras (two N-AEUs and one F-AEU) and a Data Processing System (DPS). The cameras are mounted on an optical bench which belongs

Space Telescopes and Instrumentation 2022: Optical, Infrared, and Millimeter Wave, edited by Laura E. Coyle, Shuji Matsuura, Marshall D. Perrin, Proc. of SPIE Vol. 12180, 121804M · © 2022 SPIE · 0277-786X · doi: 10.1117/12.2629189

Figure 1. Artist impression of the PLATO Spacecraft with the 26 cameras on the optical bench. The Electronic Units are hidden behind the radiator visible in front below the cameras. Credits: OHB System AG

to the spacecraft. The electronic units are accommodated separately from the cameras inside the spacecraft service module.

As detailed in Ref. 2, the 24 N-CAMs are split into 4 groups of 6 on the Spacecraft, each group being tilted by 9.2° away from the S/C Z axis (equal to the F-CAM Boresight). This allows to increase considerably the total field of view of PLATO without impacting too much the noise budget by keeping several cameras pointing to the same stars, see Ref. 3.

These 26 cameras will be used to constantly acquire stable images of thousands of star simultaneously during 4 years. By plotting the integrated flux of each star PSF over time, photometric time-series of each star can be created to evaluate the photometric variation of the star. In case of an exoplanet transit, this time-series will show a typical transit shaped drop of the integrated flux allowing the scientists to compute several parameters of the star-planet couple, such as relative size of the planet, orbit duration, orbit inclination. In combination with the asteroseismology measurements of the star itself, the age of the system and the mass of the star can also be determined.

1.2 PLATO Camera Design and Parameters

The N-CAMs are working at a nominal cadence of 25s and are optimized to monitor stars fainter than magnitude 8. The F-CAMs are working at a cadence of 2.5s and mainly observing stars in the magnitude range 4 to 8, on top of providing information for the Fine Guidance System in closed loop with the Spacecraft AOCS. Each camera is split into 3 major sub-systems: a Telescope Optical Unit (TOU), a Focal Plane Assembly (FPA) and a Front End Electronic unit (FEE).

The TOU includes a total of 6 lenses, see Fig. 2, that allows to create an image of a very large field of view of more than 18° radius, see Refs. 4, 5 for more details. A baffle is attached to the entrance protective window of the TOU to limit the straylight coming from other parts of the S/C or other cameras, and from celestial objects like the Moon or the Earth. The baffle also acts as the main thermal radiator of the camera. The TOU is attached with 3 bipods to the FPA.

The FPA offers a stable structure to support the 4 CCDs that are needed to map the very large field of view of the PLATO cameras. A conductive thermal link is in place between the FPA and the TOU to allow for thermal dissipation of the CCD heat through the Baffle. See Refs. 6 and 7 for more details on the FPA design.

Finally, the FEE unit is mechanically attached to the TOU (for the N-CAM only) and linked to the FPA via the CCD flexis cables. This unit allows reading of the CCD and acquiring of images in the given cadence and in window mode if wanted.

Further author information: Send correspondence to martin.pertenais@dlr.de

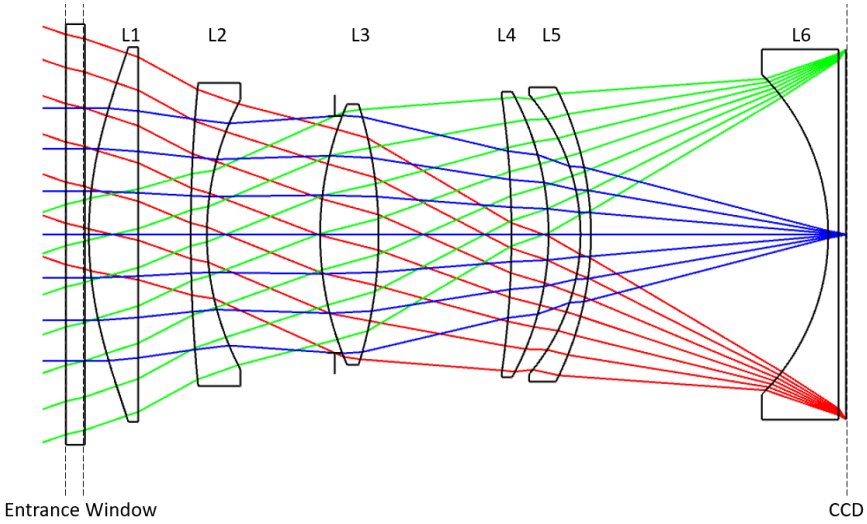

Figure 2. Optical Design of PLATO' Camera, with a protective entrance window followed by a 5-lenses imaging system and finally a last field lens few millimeters in front of the sensitive area of the CCD on the FPA.

1.3 Ghosts in PLATO cameras

What will be called ghosts or ghost images in this paper are spots or features imaged on the focal plane that are actually not present in the observed field of view (FoV), see Ref. 8 for detailed theoretical description of ghosts. In contrary to other straylight effects observed by an instrument, ghost images are generally more localized effects that have therefore different implications than a simple increase of background level due to straylight.

Ghosts in PLATO's case are unfocused duplicate of some stars that are in the camera FoV and being imaged on the FPA. They are generated by reflections between surfaces of the camera such as lenses, window or CCD. If the reflected light from a given surface is turned back again by reflection from another surface, it may travel to the focal plane to form a ghost image. The presence of Anti-Reflection (AR) coating on each lens and window is the first prevention design measure that has been taken to limit the intensity of ghosts in PLATO's cameras. Because the intensity of the light generating a ghost image is decreased by a significant factor after each reflection on a surface, the ghosts created by reflections on 2 surfaces will be the most significant.

The interest in the ghost images simulation and measurement in PLATO is driven by the potential impact they could have on the science goals. For example, if an extended ghost of a strongly variable star superimpose with a target, it will contribute to the photometry of this target and could create a false-positive planet detection.

Sect. 2 describes simulations to characterise the ghosts expected for PLATO's cameras. Sect. 3 reports the measurements taken in the first test campaign of the camera engineering model. Sect. 4 compares the results of the test campaigns to the expectations from simulations before we conclude in Sect. 5.

2. GHOST SIMULATIONS

2.1 Assumptions and Parameters

In order to perform a first order simulation and characterization of the significant ghosts for PLATO's camera, the following parameters and assumptions have been defined and used:

- Entrance pupil = 12cm
- Nominal size of the image of a star on the detector = 4x4 pixels (with a pixel pitch of 18µm)
- Total optical transmission of the window and lenses = 75%

- Anti-Reflection Coating performance = 1%
- CCD Surface Reflection = 15%

These values are considered to be the worst possible case for the ghost creation point of view. This is done in order to have a sizing cases of the ghosts. The measurements performed with the actual hardware, described in Sec. 3, will then allow us to confirm these assumptions or not.

On top of this first-order simulations, more realistic value, including reflectivity of the surface as a function of both wavelength and angle of incidence have been defined and implemented in a straylight analysis software.

2.2 Overview

The two main metrics to establish and characterize ghosts are energy (integrated flux) and their size on the detector. Ratio of both produce the final master figure of merit: the irradiance. In the worst case the ghost has high energy and is spread over a small size on the detector, leading to a high irradiance.

2.2.1 Ghosts' energy

In terms of energy and using the parameters defined in Sec. 2.1, PLATO's cameras have mainly 3 relevant ghosts, created between following surfaces:

- CCD with the Window (both surfaces)
- CCD with L6 (both S1 and S2)
- CCD with L4 Surface 1

Considering a significantly higher reflectivity of the CCD than the optical surfaces, we expect the most energetic ghosts to originate from a first reflection on the CCD. Using 15% and 1% reflectivity for the CCD and the optical surfaces respectively, and 75% optical transmission, the order of magnitude of these ghost is expected to be at least 1E-3 fainter than the original star image:

$$E_{ghost} < CCD_{reflec} \cdot Optical_{reflec} \cdot Transmission^2 \tag{1}$$

Considering that the CCD reflectivity is actually much lower for most of the wavelengths, and that a non-negligible part of the back reflected rays will be vignetted on its way to the detector, the expected energy of the ghosts is actually an order of magnitude lower. But this value of 1E-3 provides a first order maximal value of what can be expected with PLATO's cameras.

2.2.2 Ghosts' size

In terms of size, PLATO's camera have 2 so-called point-like ghosts (almost as small as their original image, $<<$ 1mm^2) and 3 main extended ghost:

- Window S1 with Window S2 ($\sim 10^{-3}$ mm^2)
- CCD with Window surfaces ($\sim 10^{-2}$ mm^2)
- CCD with L6 S2 ($\sim$ 10 mm^2)
- L6 S1 with L6 S2 ($\sim$ 10 mm^2)
- L6 S2 with Window surfaces ($\sim$ 10 mm^2)

All the other ghosts created and not listed here have a size so large that they could be considered as part of the background straylight and not as proper ghosts.

Table 1. Overview of PLATO Ghost Irradiance.

Surface 1	Surface 2	Relative Irradiance	Position
CCD	**Back of window**	**0.058%**	**symmetric wrt optical axis (-x,-y)**
Back of window	Front of window	0.039%	on top of original image
CCD	**Front of window**	**0.024%**	**symmetric wrt optical axis (-x,-y)**
CCD	**Back of L6**	**0.00003%**	**further away from the optical axis, along the same radius**
CCD	Front of L6	0.000007%	further away from the optical axis, along the same radius
Back of L6	Back of window	0.000004%	symmetric wrt optical axis (-x,-y)

2.2.3 Ghosts' irradiance

Looking at the ratio of both energy and size and listing the PLATO ghost with the highest irradiance, the 6 ghosts listed in the table 1 can be considered. Note that the values of irradiance are given as example to have again a highest worst case limit of what to expect.

The first 3 ghosts of this table are considered to be point-like ghost with very small size, explaining their very high irradiance. As it falls on top of the original image, the second ghost (created by the window itself) can be ignored for further analysis. It will create a kind of halo around each star that can be considered for photometry as part of the PSF wings for the star.

As a summary and based on this first order analysis, it was decided to consider for further simulation and measurement the point-like ghost created by the CCD and the Window (first and third of the table) and the extended ghost created by the CCD and the back of L6. All 3 ghosts are highlighted in bold text in table 1.

2.3 Extended Ghost

Figure 3 below shows the creation of the most energetic extended ghosts between the CCD and the back of L6. It is to be noted that for stars up to 6° away from the optical axis, the nominal PSF will be inside the ghost (as for the blue and green beams in Fig. 3).

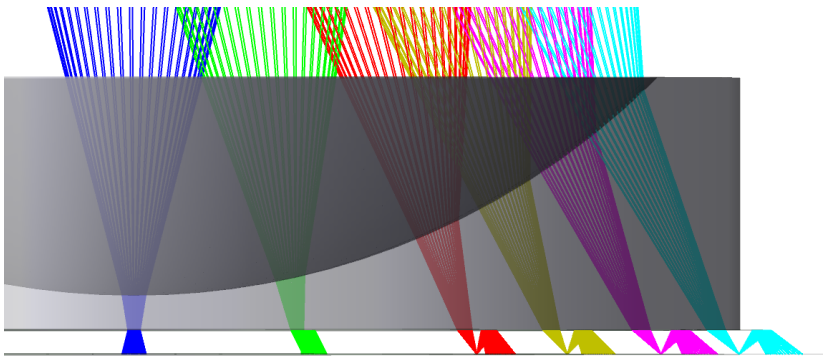

Figure 3. View of the extended ghost creation after a first reflection on the CCD (bottom surface) followed with a back-reflection on the flat exit surface of L6 (in grey). The dark blue beam in on the optical axis of the camera and the light blue at the edge of the field of view.

The centroid position of the ghost is following linearly the chief ray angle reaching the detector. After computation on Zemax, considering a factor 1.0672 between the ghost centroid and the PSF centroid in each

direction induces an error of less than 0.1 mm on the ghost centroid position. We can therefore consider: $X_{ghost} = 1.0672 * X_{PSF}$ and $Y_{ghost} = 1.0672 * Y_{PSF}$. As for the simulated size of the extended ghost, simulations show an elliptical shape of the ghost with increased eccentricity with the angle from the optical axis. Figure 4 shows the shape of the ghost for the 6 field of view positions previously simulated in Fig. 3. For first-order estimation, the size of the ghost is simulated by a circle. The left-hand side of Fig. 4 shows a polynomial fit of the evolution of the ghost radius with the angle from the optical axis.

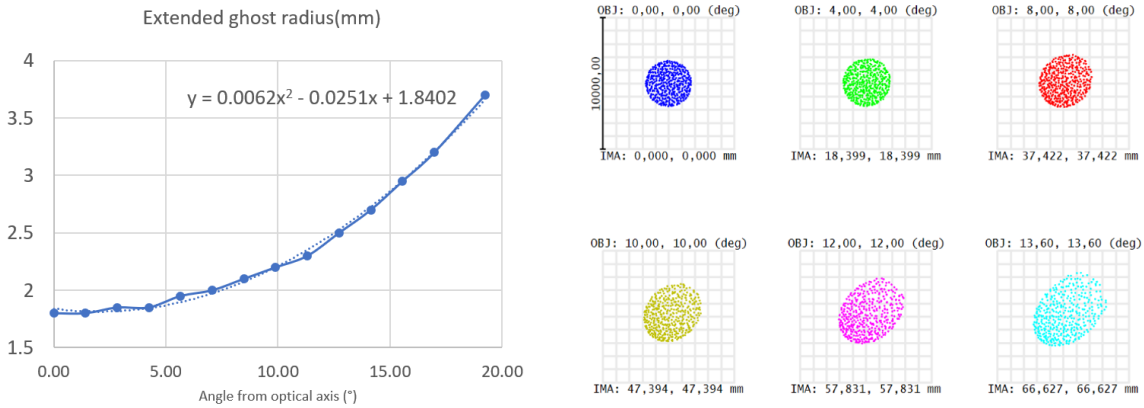

Figure 4. Simulation of the size and shape of the extended ghost. Left: circular polynomial approximation of the ghost size as a function of the angle from the optical axis. Right: example of ghost shape and intensity distribution for the 6 FoV positions from the optical axis (dark blue) up to the edge of the FoV (light blue).

Given a simulation of a star producing and irradiance of 1.6e6 W/mm2 on the detector and given the parameters of section 2.1 for the ghost computation, the optical simulations provide an absolute ghost irradiance of up to 0.5 W/mm2. That means that, in the worst case, the extended ghost is at most 0.00003% as bright as the corresponding target. This worst case occurs close to the optical axis where the ghost covers the smallest area, see Fig. 4. As an example, this value of 0.00003% goes down to 0.000017% by considering a nominal PSF focused in 3x3 pixels instead of 4x4 pixels. This gives perspective for the uncertainties of this first-order simulation.

In order to prepare for the test and train the analysis algorithm, this extended ghost was implemented in PLATOSim, the official image simulator of PLATO. This provided for example an extended ghost for a magnitude V=0 star 7° away from the optical axis of 98 photo-electrons in average per pixel per exposure.

2.4 Point-like Ghost

As described above, the main point-like ghost to consider is a super-imposition of 2 ghosts created first by a reflecting on the CCD surface and then by either surface of the parallel entrance window of the camera.

Using the same example as for the extended ghosts, each of them will have an irradiance of respectively of 952 and 390 W/mm^2. Considering a perfect super-imposition (worst case), this makes a total of 1342 W/mm^2, meaning 0.082% of the nominal image irradiance.

This means that each star (less than 8° away from the optical axis) will produce a symmetric ghost on the other side of the optical axis (on another CCD) with $\sim$ 0.082% less irradiance. Considering that the ghost is expected to be $\sim$2 times larger in term of area on the the detector than the nominal PSF, this would correspond to an integrated flux of the ghost $\sim$ 0.041% of the flux of the nominal image of the star, this is a factor of $\sim$2400.

3. GHOST MEASUREMENT

3.1 Test setup and procedure

As part of the MAIV Campaign of the Camera EM, a test setup was developed at SRON to enable the full performance testing and calibration of the PLATO Camera in operational conditions. Refs. 9, 10 summarize the setup description and overall test results.

The camera is fixed in a gimbal allowing to rotate it and access the complete scientific field of view. The fixed collimator (OGSE) illuminates the complete entrance pupil of the camera with a representative spectrum of PLATO's reference star. For the ghost dedicated test, the test procedure was defined to be as follow:

- Wait for thermal stabilisation at the nominal operational temperature
- for each FoV position:

  acquire background images

  set OGSE intensity to required value 1 (saturated exposures, close to magnitude V=1.5)

  acquire a given number of full-frame images

  set OGSE intensity to required value 2 (non-saturated exposures, close to magnitude V=8)

  acquire a given number of full-frame images

The map of the commanded FoV positions is shown in Fig. 5. One CCD (upper right quadrant in the figure) is mapped with 2 sets of 5 off-axis angles (3.8°, 7.6°, 11.4°, 15.2°, and 18.88°) for 2 different azimuths, while the remaining 3 CCDs are mapped with these 5 off-axis angles along their diagonal. Finally, the gaps (without sensitive area) between CCDs are also being illuminated in both X and Y direction, to potentially look for unexpected ghosts created by this non-sensitive area on the FPA.

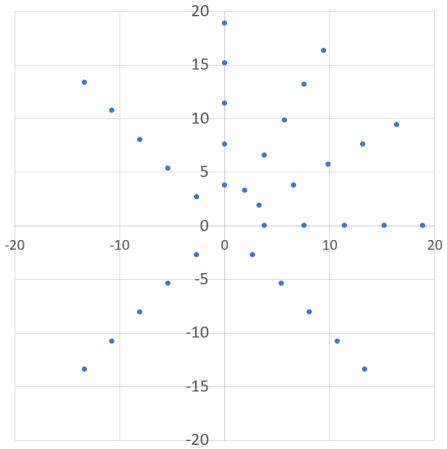

Figure 5. List of field of view points visited during the EM Ghost test. Each quadrant of this plot corresponds to 1 CCD on the FPA. Axis labels give the angle from the optical axis in degrees while the optical axis is at (0°,0°). Azimuthal angle equals zero at the bottom axis of the first quadrant as usual.

For each of these FoV positions both saturated and non-saturated exposures were acquired, thanks to a neutral density filter wheel in the OGSE. Saturated exposures were mostly used to find the ghosts and characterize the very faint extended ghosts, while the non-saturated ones were used for characterization only.

3.2 Analysis and results

3.2.1 Analysis steps

The background image for a FoV position was smoothed with a 2D boxcar kernel of 20 pixels and subtracted from the respective averaged saturated and non-saturated exposures.

The extended ghosts are very faint, even in the saturated images. Nevertheless, they can be recovered at the expected location by eye because of their large size, even though the signal is less than the average noise level. An elliptical aperture was overlaid with SAOImage DS9 version 7.3.2 to match the circumference of the extended ghost, giving the semi-major and the semi-minor axis, the area measured in number of pixels, as well as the centroid position.

The measurement of integrated flux is complicated by the faintness of the extended ghost and a variable, negative residual background flux after background subtraction. A rough estimate of the integrated flux was obtained by sampling the background flux and ghost flux in various locations, see Fig. 6, and extrapolating the difference between ghost and background flux to the size of the ghost image. The uncertainty of the background light level contributes an error bar of 20 % to the estimated flux. This partially due to a so-called tearing effect of the CCD where a drop of background level is observed in the opposite direction of reading from a saturated spot.

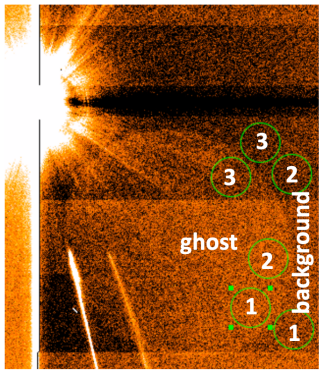

Figure 6. Local sampling of the extended ghost flux and residual background flux using small apertures with a radius of 20 pixels.

As opposed to the extended ghost, a point-like ghost with the same amount of light in a pixel would not be visible since the PLATO PSF has a size of less than 4x4 pixels only, and the ghost is expected to be around 6x6 pixels. An initial search for point-like ghosts using an automatic peak detection algorithm did not succeed. Then, the search was restricted to the recovery of the expected symmetric point-like ghosts by eye.

The integrated flux of point-like ghosts was measured from annuli in SAOImage DS9, correctly accounting for the residual background light level in faint cases. A simple integration of flux in a circular aperture was considered sufficient for the bright OGSE primary image. The flux measured in digital units was converted to number of electrons using a gain factor of 28 e^-/ADU.

3.2.2 Measurement results

The size of the extended ghost was characterised at 11.4° away from the optical axis, giving an aspect ratio of 1.09 and an area of 42,530 pixels.

The photometric measurements are listed in Table 2 for the extended ghost and and in Table 3 for the point-like ghost at the given FoV positions.

The non-saturated exposure identified in Table 3 is actually slightly saturated. A stellar flux of 5,600 ke^- was found from integration in a circular aperture, resulting in a flux ratio of 2,650±750 for the point-like ghost.

angle from line of sight	azimuthal angle	extended ghost flux [ke$^-$]
3.8°	135°	1,794.9
7.6°	135°	1,190.8
11.4°	135°	952.0
15.2°	30°	1,652.0
15.2°	60°	1,537.2

Table 2. Integrated flux of extended ghosts obtained from extrapolating local samples of ghost and background flux in saturated exposures. The ghosts were observed at different FoV positions identified by the angle from the line of sight and the azimuthal angle. An uncertainty of 20 % should be applied to all extended ghost flux measurements. The estimates for the ghost at 3.8° and 7.6° are very uncertain since only a part of the ghost is accessible outside of the primary PSF.

angle from line of sight	azimuthal angle	point-like ghost flux [ke$^-$)]		
non-saturated exposures				
3.8°	135°	2.38	±	0.70
saturated exposures				
3.8°	135°	644		
7.6°	135°	2.80	±	0.84
11.4°	135°	0.92	±	0.17

Table 3. Integrated flux of point-like ghosts. The uncertainty of residual background flux is irrelevant for very high signals so the error is omitted in the first row for the saturated case.

Close to the line of sight, the point-like ghost is clearly detectable at an off-axis angle of 3.8°. Comparing the saturated and the non-saturated exposure taken at this position of the light source, the measured fluxes of the point-like ghost marginally agree, given the magnitude difference of 6.5 (Table 3 and Sect. 3.1).

Far away from the line of sight, the point-like ghost for 135° and 11.4° is very faint with some 900 e$^-$ only. This was expected because of vignetting.

There is bright feature at an off-axis angle of 18.88°. Even though it resides roughly at the expected location of an extended ghost it is much brighter. It is a reflection of the straylight mask and will be out of the field of view of the cameras.

4. COMPARISON OF MEASUREMENTS WITH SIMULATIONS

The area expected with Zemax for the elliptical extended ghost at an angle of 11.4° from the optical axis is 13.79 mm^2, corresponding to 42,550 pixels. This fits very well the 42,530 pixels measured here, Figure 7.

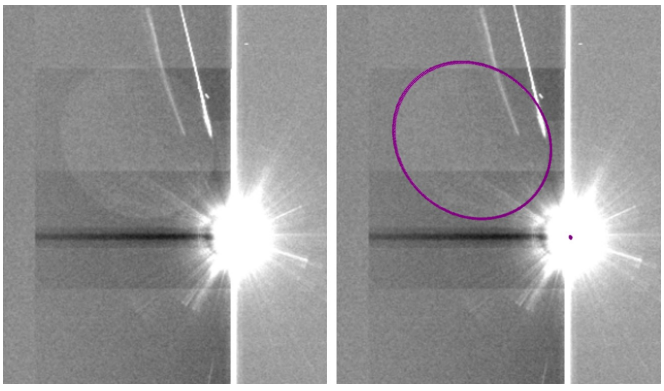

Figure 7. Comparison of a simulated ghost, as described in Sec. 2, in purple on top of an actual image acquired with the camera EM, for a saturated spot at 11.4° off-axis. A part of the observed frame centered around the OGSE image and the ghost is shown twice, once with the simulated ghost (right) and one without (left).

Similarly, the position of the ghost centroid relative to the star is very well within the expectation from the simulation, with (147, 143) absolute pixels shift in (X, Y) compared to (132, 130) simulated. This shows, as expected, that the extended ghost position and size is very deterministic and that the simulation can be fully trusted in these aspects.

As opposed to point-like ghost flux, the flux of the extended ghost is not expected to vary a lot with the angle of the OGSE from the optical axis. The measurements are consistent with the simulated decrease of ghost flux of about 10 % between off-axis angles of 1° and 16° (Table 2). Even though a precise radiometric calibration is not possible in the current test setup, the flux level of about 1,200 ke^- observed for the extended ghost at a magnitude of 1.5 and an off-axis angle of 7.6° (Table 2) would be of the order expected from simulations. Simulations indeed predicted a ghost of 3,800 ke^- integrated flux for magnitude 0 at 7° off-axis. A magnitude 0 star being 4 times brighter than a magnitude 1.5 star, this would be equivalent to 950 ke^- for a magnitude 1.5 star. Considering again the high uncertainty on the absolute radiometric flux used in the test setup, this 950 ke^- is matching well the 1,200 ke^- measured.

For the point-like ghost, there is less agreement with simulations at high off-axis angles. This is mostly due to the fact that the vignetting function across the FoV wasn't properly included in the simulation. The measured ghosts are therefore much fainter than expected. For example, a flux of some 160 ke^- was expected from simulations at an off-axis angle of 7° at the saturating magnitude of 1.5 assumed here (Sect. 3.1). The ghost location is, as simulated, symmetric w.r.t the light source (as should be) but the flux amounts to only about 3 ke^-, at an angle of 7.6° from the optical axis (see Table 3).

As noted above, the assumed magnitude of the light source is uncertain and an accurate flux calibration is not possible with the test setup. Therefore, the direct comparison of flux values to simulations is rather difficult. However, a comparison is possible for different off-axis angles on a relative scale. The flux ratio of point-like ghosts can be taken between different off-axis angles and compared to simulations.

For example, the flux ratio of 2,650±750 (Sec. 3.2.2) measured for the point-like ghost from the non-saturated exposure at an off-axis angle of 3.8° (between the stellar flux and its ghost) is in good agreement within error bars with the simulated value of ∼2,400 (Sect. 2.4). This relative measurement between the star and its ghost allows us to remove most of the uncertainties due to the absolute radiometric calibration, assumptions on vignetting and gain. It therefore confirms well that our measurements are in-line with the expected simulated ghosts.

5. CONCLUSION AND OUTCOME

This article first presented the relevant ghosts that were identified for the PLATO mission. As per simulations described here, none of these ghosts are considered to potentially harm the science objectives of the mission. In order to verify this and gain confidence on the assumptions taken, a test setup was developed and described here. The results of the tests perform on the camera EM confirmed our simulations to most extent:

The extended ghosts match preparatory simulations very well. In terms of size and positions, the measured ghosts correspond exactly to the ones simulated, confirming their deterministic characteristic. In terms of intensity, we showed that the order of magnitude of integrated flux inside this extended ghost corresponds well to the one simulated, within error bars due to the unaccuracy of the absolute radiometric calibration of the setup. The ghosts were too faint to perform a reliable relative comparison of the irradiance with the stellar one. This is a good sign, giving hints that the assumptions taken in the simulations are real worst cases.

As for the point-like ghosts, their position and size also match perfectly the predicted ones. Their flux ratio amounts to about 2,700 at an off-axis angle of 3.8° which is within error bars of the simulated flux ratio with the nominal stellar flux.

Finally, no other significant unexpected ghosts were discovered. Looking at the highly saturated exposures, a faint halo could be observed around the star image by playing with the image contrast. This corresponds to the ghost created by both sides of the window (second line of table 1). As visible in Fig. 7, a couple of long stripes pointing at the saturated spot were observed. The team is still investigating to understand if these come from the setup OGSE or are a reflection within the camera. The final test using the Flight Model (FM) camera should help identifying the root-cause.

ACKNOWLEDGMENTS

This work presents results from the European Space Agency (ESA) space mission PLATO. The PLATO payload, the PLATO Ground Segment and PLATO data processing are joint developments of ESA and the PLATO Mission Consortium (PMC). Funding for the PMC is provided at national levels, in particular by countries participating in the PLATO Multilateral Agreement (Austria, Belgium, Czech Republic, Denmark, France, Germany, Italy, Netherlands, Portugal, Spain, Sweden, Switzerland, Norway, and United Kingdom) and institutions from Brazil. The authors thank the Belgian Federal Science Policy Office (BELSPO) for the provision of financial support in the framework of the PRODEX Programme of the European Space Agency (ESA) under contract number PEA 4000137604. M.A. acknowledges support from the German Aerospace Center (DLR FKZ 50OP1902). Members of the PLATO Consortium can be found at https://platomission.com/. The ESA PLATO mission website is https://www.cosmos.esa.int/plato. We thank the teams working for PLATO for all their work.

REFERENCES

[1] Rauer, H., Catala, C., Aerts, C., Appourchaux, T., Benz, W., Brandeker, A., Christensen-Dalsgaard, J., Deleuil, M., Gizon, L., Goupil, M.-J., and et al., "The plato 2.0 mission," *Experimental Astronomy* **38**, 249–330 (Sep 2014).

[2] Pertenais, M., Cabrera, J., Paproth, C., Boerner, A., Griessbach, D., Mogulsky, V., and Rauer, H., "The unique field-of-view and focusing budgets of PLATO," in [*International Conference on Space Optics — ICSO 2020*], Cugny, B., Sodnik, Z., and Karafolas, N., eds., **11852**, 2043 – 2054, International Society for Optics and Photonics, SPIE (2021).

[3] Ragazzoni, R., Magrin, D., Rauer, H., Pagano, I., Nascimbeni, V., Piotto, G., Piazza, D., Levacher, P., Schweitzer, M., Basso, S., Bandy, T., Benz, W., Bergomi, M., Biondi, F., Boerner, A., Borsa, F., Brandeker, A., Brändli, M., Bruno, G., Cabrera, J., Chinellato, S., Roche, T. D., Dima, M., Erikson, A., Farinato, J., Munari, M., Ghigo, M., Greggio, D., Gullieuszik, M., Klebor, M., Marafatto, L., Mogulsky, V., Peter, G., Rieder, M., Sicilia, D., Spiga, D., Viotto, V., Wieser, M., Heras, A. M., Gondoin, P., Bodin, P., and Catala, C., "PLATO: a multiple telescope spacecraft for exo-planets hunting," in [*Space Telescopes and Instrumentation 2016: Optical, Infrared, and Millimeter Wave*], MacEwen, H. A., Fazio, G. G., Lystrup, M., Batalha, N., Siegler, N., and Tong, E. C., eds., **9904**, 731 – 737, International Society for Optics and Photonics, SPIE (2016).

[4] Magrin, D., Munari, M., Pagano, I., Piazza, D., Ragazzoni, R., Arcidiacono, C., Basso, S., Dima, M., Farinato, J., Gambicorti, L., Gentile, G., Ghigo, M., Pace, E., Piotto, G., Scuderi, S., Viotto, V., Zima, W., and Catala, C., "PLATO: detailed design of the telescope optical units," in [*Space Telescopes and Instrumentation 2010: Optical, Infrared, and Millimeter Wave*], Jr., J. M. O., Clampin, M. C., and MacEwen, H. A., eds., **7731**, 715 – 722, International Society for Optics and Photonics, SPIE (2010).

[5] Magrin, D., "Plato telescope optical units: An update on working status," in [*Space Telescopes and Instrumentation 2020: Optical, Infrared, and Millimeter Wave*], *Society of Photo-Optical Instrumentation Engineers (SPIE) Conference Series* **11443-80** (2020).

[6] Moreno, J., Vielba, E., Manjón, A., Motos, A., Vázquez, E., Rodríguez, E., Saez, D., Sengl, M., Fernández, J., Campos, G., Muñoz, D., Mas, M., Balado, A., Ramos, G., Cerruti, C., Pajas, M., Catalán, I., Alcacera, M. A., Valverde, A., Pflueger, P., and Vera, I., "PLATO FPA. focal plane assembly of PLATO instrument," in [*International Conference on Space Optics; ICSO 2018*], *Society of Photo-Optical Instrumentation Engineers (SPIE) Conference Series* **11180**, 111803N (July 2019).

[7] Ramos, G., Guijarro, A. L. V., Rodrigo, M. T., Sierra, M. A., Gómez, L. J., Borreguero, E., Álvarez, L., Manjón, A., Balado, A., Barrado, D., and Mas, J. M., "Planetary transits and oscillation of stars (PLATO) focal plane assembly (FPA): prototype assembly and integration verification," in [*UV/Optical/IR Space Telescopes and Instruments: Innovative Technologies and Concepts IX*], Barto, A. A., Breckinridge, J. B., and Stahl, H. P., eds., **11115**, 49 – 59, International Society for Optics and Photonics, SPIE (2019).

[8] Murray, A. E., "Reflected light and ghosts in optical systems," *J. Opt. Soc. Am.* **39**, 30–35 (Jan 1949).

[9] Gorius, N. and et al., "Status of PLATO mission camera: recent progress on the camera engineering model and MAIV approach for the camera flight models," in [*Society of Photo-Optical Instrumentation Engineers (SPIE) Conference Series*], *Society of Photo-Optical Instrumentation Engineers (SPIE) Conference Series* **12180**, 1218046 (Dec. 2022).

[10] Borsa, F., Gorius, N., Cottinelli, A., and et al., "PLATO EM cryogenic vacuum test campaign results," in [*Society of Photo-Optical Instrumentation Engineers (SPIE) Conference Series*], *Society of Photo-Optical Instrumentation Engineers (SPIE) Conference Series* **12180**, 1218050 (Dec. 2022).